Check for updates

MATERIALS SCIENCE

Sequential multidimensional heteroepitaxy of chalcogen-sharing 3D ZnSe and 2D $MoSe_2$ with quasi van der Waals interface engineering

Suhyun Kim[1]†, Saeyoung Oh[2]†, Seung Jae Kwak[3]†, Gichang Noh[1]†, Minhyuk Choi[4], Jaehyun Lee[1], Yuseok Kim[1], Min-gyu Kim[1], Tae Soo Kim[1], Min-kyung Jo[1,4], Won Bo Lee[3], Jinkyoung Yoo[5], Young Joon Hong[6], Seungwoo Song[4], Joon Young Kwak[7]*, YongJoo Kim[8]*, Hu Young Jeong[9]*, Kibum Kang[1,2]*

Copyright © 2025 The Authors, some rights reserved; exclusive licensee American Association for the Advancement of Science. No claim to original U.S. Government Works. Distributed under a Creative Commons Attribution NonCommercial License 4.0 (CC BY-NC).

Two-dimensional (2D) materials are emerging as a promising platform for epitaxial growth, largely free from the constraints of lattice constant and thermal expansion coefficient mismatches. Among them, transition metal dichalcogenides (TMDs), known for their superior electrical properties, are ideal for ultrathin semiconductor applications. Their unique epitaxial characteristics enable seamless integration with 3D materials, facilitating the development of gate stacks and heterojunction devices. In this regard, developing a process for growing high-quality 3D epitaxial materials before and after the growth of 2D TMDs and understanding the 2D/3D interface are crucial. This study demonstrates the sequential growth of fully epitaxial ZnSe/$MoSe_2$/ZnSe heterostructures using metal-organic chemical vapor deposition. ZnSe and $MoSe_2$, sharing chalcogen elements, enable large-area quasi van der Waals epitaxy with sharp interfaces without intermediate phase. Multiscale analysis involving transmission electron microscopy and density functional theory calculation reveals lattice commensurability, van der Waals gaps, termination, and interfacial reconstruction. Understanding these interactions is crucial for advancing multidimensional integration of 2D and 3D materials.

INTRODUCTION

Heteroepitaxy is crucial in the semiconductor industry for developing advanced devices by integrating materials with different properties (*1*–*5*). Successfully matching lattice constants and thermal expansion coefficients minimizes interface strain and prevents defects, which are vital for maintaining the electronic properties and functionality of devices. The advent of two-dimensional (2D) van der Waals (vdW) materials has revolutionized traditional heteroepitaxy, giving rise to vdW epitaxy, which involves epitaxial growth between layered materials (*6*–*8*), and quasi vdW (QvdW) epitaxy, where layered materials are combined with bulk materials that have dangling bonds (*9*–*11*). These innovative methods facilitate the growth of materials with mismatched lattice constants and thermal expansion coefficients by using the weak vdW forces between layers, thus eliminating the need for strict matching and enhancing flexibility in material combination for groundbreaking device designs.

Among the 2D vdW materials, the exploration of 2D transition metal dichalcogenides (2D TMDs), key semiconductor substances, has notably advanced the potential of vdW epitaxy and QvdW epitaxy. Multiheterojunction using 2D TMDs shows promise for applications in quantum devices (*12*–*17*), 3D integrated transistor devices (*18*, *19*), and tandem solar cells (*20*–*22*). Moreover, for the application of 2D TMDs in next-generation logic channels, it is crucial to develop a process that supports the growth of high-quality 3D epitaxial materials both before and after the deposition of 2D TMDs. Since 2D materials, which are often vulnerable to external environments, cannot typically be used alone, it is necessary to combine them with rigid 3D materials. Our focus on 2D/3D interactions was motivated by the need to understand their fundamental interactions. Understanding the 2D/3D interface, surface termination, and atomic-level reconstruction is essential for effectively engineering the electrical and optical properties of 2D TMDs (*23*, *24*). However, achieving sequential growth in multiheterojunction QvdW epitaxy presents challenges, particularly when depositing 3D nitrides or oxides on 2D TMDs. This is due to harsh growth conditions, such as the high temperatures exceeding 1000°C required for epitaxial GaN growth to decompose NH_3 precursors. In addition, even lower-temperature processes like atomic layer deposition of oxides or nitrides adversely affect 2D TMDs due to oxidizing atmospheres or plasma-induced damage (*25*, *26*). These conditions can damage the 2D layers due to chalcogen vacancy formation, oxidation, or nitridation—all critical issues considering the surface-sensitive nature of 2D materials (*27*–*29*). Furthermore, high temperatures required for 2D TMD crystal growth exacerbate these challenges, limiting development to single heterojunctions such as MoS_2 on GaN (*30*) or GaN on WS_2 (*27*, *28*). While systematic growth studies on 2D materials using the transfer process have been demonstrated, they often result in varying interface qualities, influenced by the intricacies of the

[1]Department of Materials Science and Engineering, Korea Advanced Institute of Science and Technology (KAIST), Daejeon 34141, Republic of Korea. [2]Graduate School of Semiconductor Technology, Korea Advanced Institute of Science and Technology (KAIST), Daejeon 34141, Republic of Korea. [3]School of Chemical and Biological Engineering and Institute of Chemical Process, Seoul National University, Seoul 08826, Republic of Korea. [4]Operando Methodology and Measurement Team, Korea Research Institute of Standards and Science (KRISS), Daejeon 34113, Republic of Korea. [5]Center for Integrated Nanotechnologies, Los Alamos National Laboratory, Los Alamos, NM 87545, USA. [6]Department of Nano Engineering and Department of Nano Science and Technology, SKKU Advanced Institute of Nanotechnology (SAINT), Sungkyunkwan University, Suwon 16419, Republic of Korea. [7]Division of Electronic and Semiconductor Engineering, Ewha Womans University, Seoul 03760, Republic of Korea. [8]Department of Materials Science and Engineering, Korea University, Seoul 02841, Republic of Korea. [9]Graduate School of Semiconductor Materials and Devices Engineering, Ulsan National Institute of Science and Technology (UNIST), Ulsan 44919, Republic of Korea.
*Corresponding author. Email: kibumkang@kaist.ac.kr (K.K.); hulex@unist.ac.kr (H.Y.J.); cjyjee@korea.ac.kr (YongJoo Kim); jykwak@ewha.ac.kr (J.Y.K.)
†These authors contributed equally to this work.

Downloaded from https://www.science.org at EWHA Womans University on May 25, 2025

material transfer process (*27*–*29*, *31*, *32*). This method can lead to issues such as contamination, cracks, and wrinkles in the 2D material, which are more critical than the inconsistencies of the transfer technique and highlight the challenges of compatibility with industrial processes. In this study, we aim to address these challenges by investigating the fundamental aspects of a 3D ZnSe/2D $MoSe_2$/3D ZnSe multidimensional heterostructure (MDH) epitaxial film fabricated through a sequential metal-organic chemical vapor deposition (MOCVD) process. This exclusive transfer-free MOCVD-based sequential growth process enables the formation of 3D/2D/3D MDH structures simply by controlling the metal precursors, demonstrating a scalable and industry-compatible approach for integrating 2D and 3D materials. $MoSe_2$ and ZnSe were chosen as representative 2D and 3D materials, respectively. Investigating their integration provides valuable insights into the fundamental mechanisms of 2D/3D QvdW epitaxy, which can be extended to other material systems relevant to logic devices. Specifically, we aim to emphasize the importance of the interlayer at the 2D/3D interface, which becomes increasingly critical as device dimensions shrink. Similar to how an interlayer exists between high-*k* dielectrics and the silicon channel in conventional logic devices (e.g., the $Si/SiO_2/HfO_2$ system), finding suitable interface materials is essential for optimizing device performance in 2D material-based electronics. By studying the ZnSe/$MoSe_2$/ZnSe heterostructure, we focus on combinations of 2D and 3D materials to explore the fundamental mechanisms governing their epitaxial growth and interface formation, rather than on thickness control of the interlayer. Our choice of $MoSe_2$ and ZnSe is strategic because they share the chalcogen element selenium, which minimizes interfacial defects and adverse chemical reactions during growth, ensuring high-quality interfaces. This Se-based interface is crucial for achieving seamless integration and enhancing the structural and electronic properties of the heterostructure. Moreover, their immiscibility and the ability to directly grow 2D material on 3D material and 3D material on 2D material allow for the formation of sharp 2D/3D interfaces without the formation of secondary phases. In addition, the Se-based growth conditions without oxygen eliminate the possibility of oxidation. By forming a 3D/2D/3D MDH rather than a 2D/3D single heterostructure, we built a platform that can analyze not only 2D on 3D but also 3D on 2D heterogeneous interfaces. The atomic-resolution visualization of the heterointerfaces confirmed the incommensurateness of QvdW epitaxy between ZnSe and $MoSe_2$ with a ratio of 5 to 6. The origin of QvdW epitaxy was identified through polarity analysis. Because of the presence of 2D material, the film could be delaminated from the substrate, and the delamination behavior was analyzed to confirm the differences in the interaction of the 2D/3D interface depending on the interface constituent elements. Our results would improve the understanding of QvdW interactions of 2D and 3D materials and pave the way for implementing multidimensional integration based on 2D and 3D materials.

RESULTS

Figure 1 (A to C) provides thermodynamic and material structural backgrounds to illustrate why $MoSe_2$ and ZnSe are ideal combinations for demonstrating sequential MOCVD growth mediated by the QvdW epitaxy of MDH. Figure 1A shows the Zn-Mo-Se ternary phase diagram at 773 K, our MDH growth temperature (*33*, *34*). At this temperature, the phase diagram reveals that the only thermodynamically stable selenide phases present are ZnSe and $MoSe_2$, with no intermediate alloy phase existing within the Zn-Mo-Se ternary system. This suggests a limited possibility for the formation of intermediate phases at the heterointerface between ZnSe and $MoSe_2$. Therefore, the formation of a sharp heterointerface between ZnSe and $MoSe_2$ is thermodynamically predicted. Figure 1 (B and C) shows crystal structures of ZnSe and $MoSe_2$, respectively. ZnSe has a nonlayered 3D structure with a zincblende configuration, while $MoSe_2$ exhibits a layered 2D structure with a trigonal prismatic configuration. Despite the 17.9% primitive lattice mismatch between ZnSe and $MoSe_2$, ZnSe in the [111] direction and $MoSe_2$ in the [0001] direction share the same threefold symmetry, and the supercell matching reduces the effective mismatch to 1.5%. In conventional epitaxy, large lattice mismatches hinder epitaxial growth (*35*). Several recent studies have shown that rotated or supercell configurations can form to accommodate substantial mismatches (*36*). These configurations often result in a high density of lattice defects and dislocations, degrading the overall material quality. In contrast, QvdW epitaxy mode accommodates the threefold symmetry and vdW surface mediation. Figure 1D shows a schematic image that describes the sequential MOCVD growth of ZnSe/$MoSe_2$/ZnSe on GaAs (111) substrate. The bottom ZnSe layer is grown by conventional heteroepitaxy on GaAs (111), and the top ZnSe layer is grown by the QvdW epitaxy on the $MoSe_2$ layer (discussed in Fig. 4). The details of the growth process are provided in Materials and Methods.

The atomic-scale ZnSe/$MoSe_2$/ZnSe interface was investigated on the basis of transmission electron microscopy (TEM) characterization. Figure 1E shows a representative ZnSe/$MoSe_2$/ZnSe interface image through cross-sectional high-angle annular dark field scanning transmission electron microscopy (HAADF-STEM) viewed along the $[11\bar{2}]_{ZnSe}$. It shows that the two types of ZnSe regions are separated by bilayer $MoSe_2$ and have atomically abrupt 2D/3D interfaces. Most areas exhibited bilayer characteristics, although regions with monolayer or trilayer $MoSe_2$ were occasionally observed. Also, energy-dispersive x-ray spectroscopy (EDS) shows the elemental composition of the interface region (fig. S1). The characteristic x-ray signal of Se atoms is distributed over the entire area. The x-ray signal of Zn atoms is confined in the ZnSe region while that of Mo atoms is confined in the $MoSe_2$ region. We confirm the atomically sharp 3D/2D/3D interface through the EDS mapping images.

Figure 2 displays the structural analysis results of the 3D ZnSe/2D $MoSe_2$/3D ZnSe MDH epitaxial film on GaAs (111)B substrate. Surface morphology of ZnSe/$MoSe_2$/ZnSe MDH on GaAs (111)B is shown in fig. S2. Initially, vertical structural analysis was conducted on ZnSe/$MoSe_2$/ZnSe MDH (Fig. 2A). Raman spectroscopy and x-ray diffraction (XRD) 2θ-ω scan were performed to confirm the phases and crystal planes of the MDH. Figure 2B shows the Raman spectroscopy measurement result of ZnSe/$MoSe_2$/ZnSe on GaAs (111)B. The Raman spectrum shows peaks at 204 and 250 cm^{-1} of ZnSe and 241 cm^{-1} of $MoSe_2$, respectively (*37*, *38*). We confirm the existence of ZnSe and $MoSe_2$ without any other intermediate phase through Raman spectra. Figure 2C is a high-resolution x-ray diffraction (HR-XRD) 2θ-ω scan result for ZnSe/$MoSe_2$/ZnSe on GaAs (111)B. In the XRD 2θ-ω scan, the diffraction peaks related with the (111) plane of ZnSe and (0001) plane of $MoSe_2$ are detected. The peak at 27.25° corresponds to the ZnSe (111) diffraction peak and the peak at 56.13° to the ZnSe (222) diffraction peak (fig. S3). The

Downloaded from https://www.science.org at EWHA Womans University on May 25, 2025

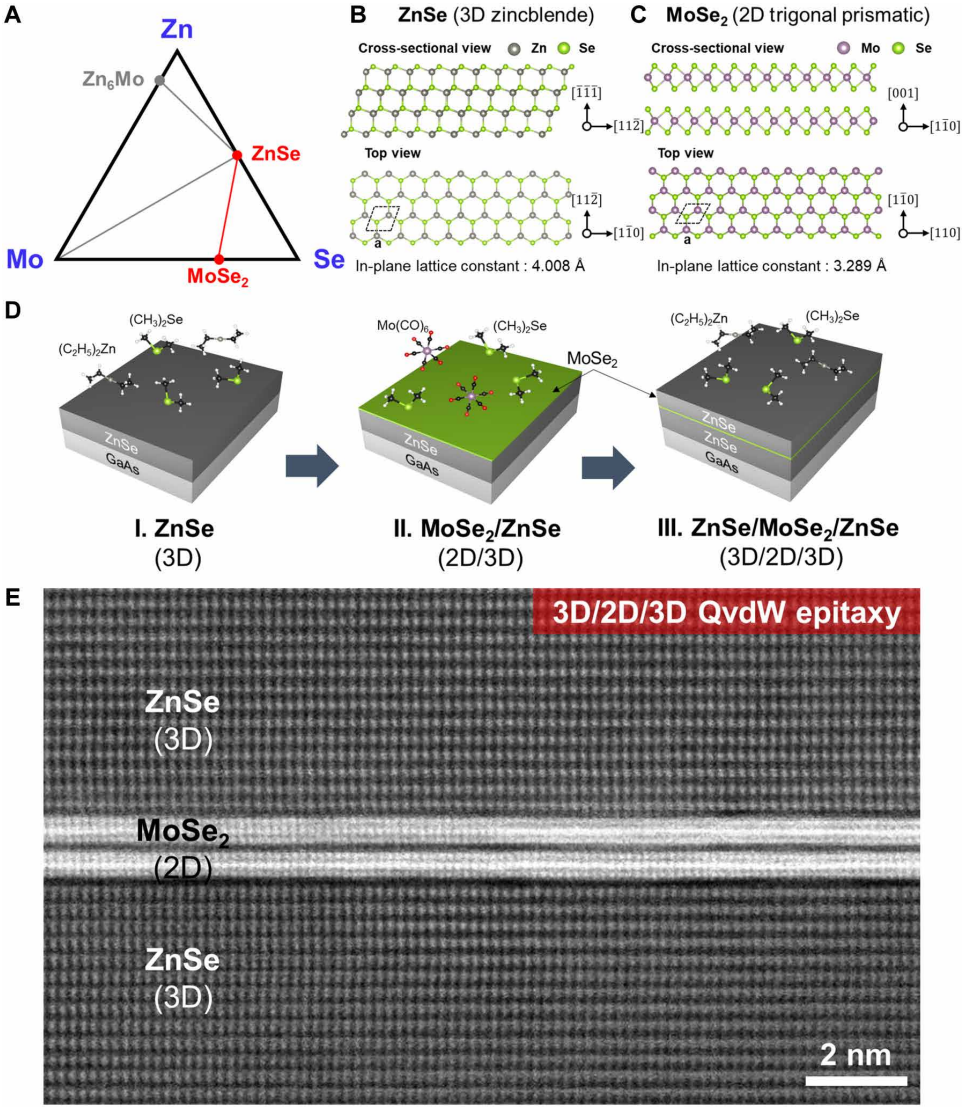


Fig. 1. Sequential MOCVD growth of ZnSe/$MoSe_2$/ZnSe MDH and its multidimensional heterointerface. (**A**) Schematic of Zn-Mo-Se ternary phase diagram at 773 K. (**B** and **C**) Crystal structure of (B) ZnSe and (C) $MoSe_2$. (**D**) Schematic diagram of the growth process of ZnSe/$MoSe_2$/ZnSe MDH on GaAs. (**E**) Cross-sectional HAADF-STEM image of ZnSe/$MoSe_2$/ZnSe MDH interface viewed along the $[11\bar{2}]_{ZnSe}$ zone axis.

positions of the ZnSe XRD peaks were consistent with those of cubic ZnSe [Joint Committee on Powder Diffraction Standards (JCPDS) no. 03-065-9602]. We confirm that both top and bottom ZnSe of the MDH grow (111)-oriented in the out of plane direction. The electron backscattered diffraction (EBSD) mapping images of the ZnSe/$MoSe_2$/ZnSe MDH are shown in Fig. 2D. Through EBSD analysis, we confirm that ZnSe grown on $MoSe_2$ has a uniform crystal orientation over a large area not only in the out of plane direction but also in the in-plane direction. Cross-sectional structural analysis of ZnSe/$MoSe_2$/ZnSe samples was then performed (Fig. 2E). Figure 2 (F and G) shows low-magnification bright-field (BF)–STEM and HAADF-STEM images, respectively. It is confirmed that $MoSe_2$ is continuous in a large area and that ZnSe exists in the form of a thin film (fig. S4). The selected area electron diffraction (SAED) pattern at the ZnSe/$MoSe_2$/ZnSe interface region is shown in Fig. 2H, with SAED patterns acquired from the area indicated in Fig. 2G. The SAED pattern shows only a single pattern corresponding to ZnSe viewed along the $[11\bar{2}]_{ZnSe}$ zone axis (Z.A.). In this SAED analysis, the electron beam diameter irradiating the selected area was 150 nm. Since the volume occupied by $MoSe_2$ was relatively small compared to ZnSe, no signal from $MoSe_2$ was detected. It is the sum of the diffraction signals from both sides of the ZnSe layer. Through the SAED pattern, we confirm that the bottom and top ZnSe have the same crystallographic orientations without distortion from each other. Together with the previous atomic-scale TEM analysis, large scale characterization results presented in Fig. 2 confirm the 3D ZnSe/2D $MoSe_2$/3D ZnSe MDH as an epitaxial film across multiple scales.

QvdW epitaxially grown films often exhibit weak interactions at the interfaces, allowing for potential film delamination and application of the transfer process. In our ZnSe/$MoSe_2$/ZnSe MDH, the interface between the $MoSe_2$ and bottom ZnSe layer shows the

Downloaded from https://www.science.org at EWHA Womans University on May 25, 2025

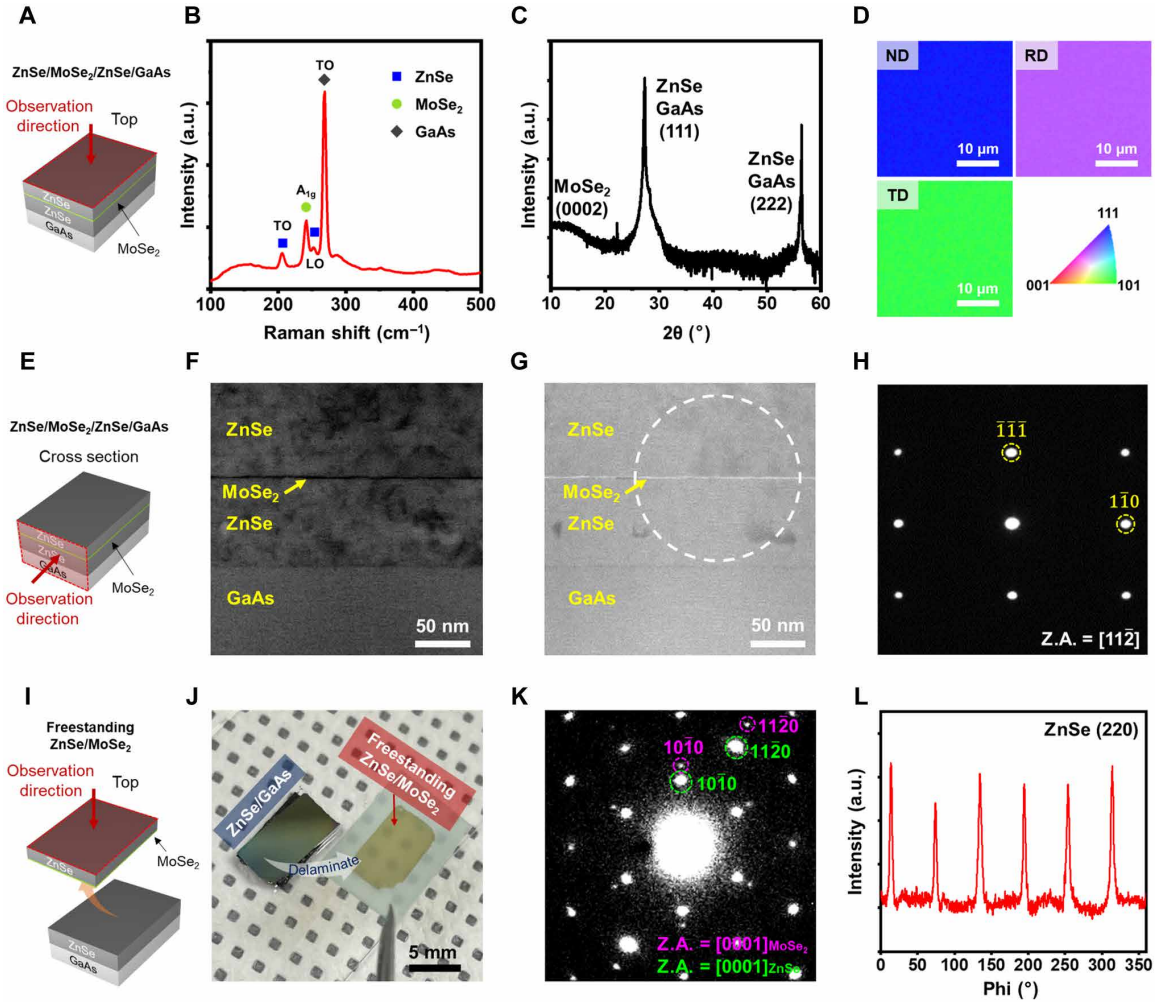


Fig. 2. Structural analysis of ZnSe/$MoSe_2$/ZnSe MDH. (**A**) Schematic of ZnSe/$MoSe_2$/ZnSe MDH and vertical analysis direction. (**B**) Raman spectra of ZnSe/$MoSe_2$/ZnSe on GaAs (111)B. (**C**) 2θ-ω scan in HR-XRD measurement of ZnSe/$MoSe_2$/ZnSe on GaAs (111)B. (**D**) EBSD inverse pole figure maps of the ZnSe/$MoSe_2$/ZnSe on GaAs (111)B surface in the normal direction (ND), transverse direction (TD), and rolling direction (RD). (**E**) Schematic of ZnSe/$MoSe_2$/ZnSe MDH and cross-sectional analysis direction. (**F**) Low-magnification cross-sectional BF-STEM image of ZnSe/$MoSe_2$/ZnSe MDH interface. (**G**) Low-magnification cross-sectional HAADF-STEM image of ZnSe/$MoSe_2$/ZnSe MDH interface. (**H**) SAED pattern obtained at the ZnSe/$MoSe_2$/ZnSe MDH interface. (**I**) Schematic of ZnSe/$MoSe_2$ sample and in-plane characterization direction. (**J**) Photographs of ZnSe/$MoSe_2$ film delaminated from ZnSe/GaAs (111)B substrate. (**K**) The SAED patterns from the delaminated ZnSe/$MoSe_2$. (**L**) HR-XRD (220) φ-scan of delaminated ZnSe/$MoSe_2$ film on TRT. a.u., arbitrary units. Z.A., zone axis.

weakest interaction (with additional details provided in Fig. 4). On the basis of this interface, the top ZnSe/$MoSe_2$ heterostructure film can be delaminated from the substrate using thermal release tape (TRT), as demonstrated in Fig. 2 (I and J). Subsequent to delamination, the ZnSe/$MoSe_2$ film was transferred onto a TEM grid, facilitating the observation of SAED patterns, as shown in Fig. 2K. Notably, the SAED patterns exclusively exhibited single hexagonal diffraction patterns of both ZnSe and $MoSe_2$, aligned in identical orientations. Through meticulous analysis of these SAED patterns, the epitaxial relationship between wurtzite (WZ) ZnSe $(000\bar{1})[11\bar{2}0]$ and $MoSe_2$ $(0001)[11\bar{2}0]$ {or zinc-blende (ZB) ZnSe $(\bar{1}\bar{1}\bar{1})[1\bar{1}0]$ and $MoSe_2$ $(0001)[11\bar{2}0]$} was firmly established. In instances where pure ZB ZnSe growth occurs along the [111] direction, the presence of a diffraction spot corresponding to the $(10\bar{1}0)$ plane would not be anticipated (fig. S5). However, because of the presence of twinned crystallites resulting in a mixture of WZ phase, such spots are observed. This is because where ZB ZnSe growth occurs along the [111] direction, ZnSe exhibits the composition of twinned crystallites relative to the substrate, serving to alleviate elastic strain within the film (*39*). Stacking faults and twinning are frequently observed in materials with ZB structure that grow along the {111} direction, even in cases of minimal lattice mismatch (*40*–*42*). This phenomenon occurs because of the inherent instability of atomic stacking sequences along the {111} planes, which are prone to slight misalignments during crystal growth. These misalignments can result in stacking faults and twin defects, acting as mechanisms to relieve internal strain and reduce the system's overall energy. ZnSe deposited atop $MoSe_2$ manifests as a mixture of ZB and WZ phases. Figure 2L presents the XRD phi-scan of the delaminated ZnSe/$MoSe_2$ film on TRT. This phi scan, conducted on the (220) plane of ZnSe, revealed six peaks characterized by a 60° interval, indicative of an in-plane registry showcasing sixfold symmetry. This sixfold symmetry

Downloaded from https://www.science.org at EWHA Womans University on May 25, 2025

outcome aligns consistently with the observations illustrated in Fig. 2K, attributed to twin formation.

To investigate the in-plane crystal information of $MoSe_2$, top-view TEM characterization was performed on the $MoSe_2$ film delaminated from the QvdW epitaxially grown 2D $MoSe_2$ on 3D ZnSe. The $MoSe_2$/ZnSe heterostructure on GaAs (111)B was prepared using the same growth process, excluding the final ZnSe layer growth step. The $MoSe_2$ film was subsequently transferred onto a holey carbon TEM grid (Fig. 3A). In Fig. 3B, the SAED pattern of the $MoSe_2$ film on the TEM grid is presented, demonstrating a singular pattern of hexagonal symmetry characteristic of $MoSe_2$. In addition, SAED patterns from nine distinct positions of the $MoSe_2$ film, as marked in Fig. 3A, are provided in fig. S6. Across various spots, the SAED patterns exhibit diffraction patterns with identical orientations and are devoid of any distortions, indicative of epitaxial growth of $MoSe_2$ on ZnSe over a substantial area. In addition, bilayer $MoSe_2$ can manifest two distinct stacking orders: AA and AB configurations (Fig. 3C). STEM images of AA stacked and AB stacked bilayer $MoSe_2$ are presented in Fig. 3 (D and E), respectively. The grain boundary between the AA stacked area and the AB stacked area is displayed in Fig. 3F. Notably, the grain boundary area of the QvdW epitaxial $MoSe_2$ film is stitched without breaking. These findings confirm the successful QvdW epitaxial growth of the bidirectional bilayer $MoSe_2$ domain on a ZnSe substrate over a large area.

To thoroughly investigate the 3D/2D/3D interface, we conducted atomic-scale observations of the ZnSe/$MoSe_2$/ZnSe structure, comparing the dependence on substrate orientation. STEM provides atomic-scale resolution and is highly sensitive to structural changes at the interface compared to measurements that provide average structure information for the entire film thickness, such as XRD. Figure 4B presents a cross-sectional heterointerface image acquired via HAADF-STEM, oriented along the $[1\bar{1}0]$ axis of ZnSe. We found that the epitaxial relationship between $MoSe_2$ and ZnSe mirrors that observed on GaAs (111)B substrates, indicating consistent growth behavior across different substrates (*43*). As further validated in Fig. 2K, we also confirm the epitaxial relationship of top ZnSe $(\bar{1}\bar{1}\bar{1})[1\bar{1}0]_{ZB-ZnSe} \parallel (0001)[11\bar{2}0]_{MoSe2}$ through HAADF-STEM as well. Despite the presence of the $MoSe_2$ layer, both the bottom and top ZnSe layers exhibit identical crystal orientations. While atomically incommensurate, our analysis reveals the formation of a commensurate supercell comprising five ZnSe lattices and six $MoSe_2$ lattices. This finding was corroborated by an inverse fast Fourier transform image (fig. S7). The QvdW gap between the bottom ZnSe and $MoSe_2$ was measured to be 0.347 nm while that between the top ZnSe and $MoSe_2$ was measured to be 0.312 nm. In HAADF-STEM imaging, signal intensity is approximately proportional to the square of the atomic number (Z) (*44*). For the ZnSe, the atomic number of Zn is 30, and the atomic number of Se is 34. So bright ones are Se atoms. The bottom ZnSe grown by conventional heteroepitaxy shows Se-terminated surface affected by As-terminated GaAs (111)B substrate. The top ZnSe exhibits the same Se-terminated surface (Fig. 4A). The interface area of the bottom ZnSe shows the same configuration as the internal bulk area. In the case of the upper ZnSe grown on $MoSe_2$, the interfacial monolayer region of the ZnSe shows a buckling structure. This phenomenon arises from the surface reconstruction of the ZnSe (111)A due to

Downloaded from https://www.science.org at EWHA Womans University on May 25, 2025

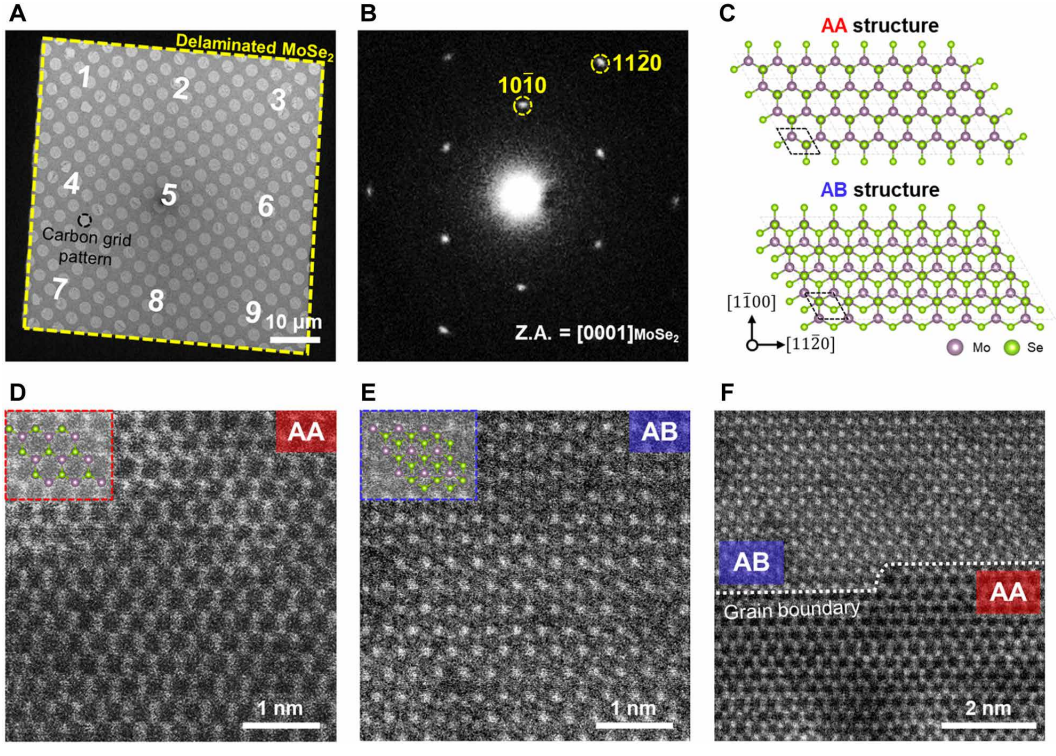


Fig. 3. Top view TEM characterizations of twinned QvdW epitaxially grown $MoSe_2$ film on ZnSe/GaAs (111)B. (**A**) Low-magnification TEM image of QvdW epitaxial grown $MoSe_2$ film on holey carbon TEM grid. (**B**) SAED patterns from the QvdW epitaxial grown $MoSe_2$ film. (**C**) Lattice configurations of AA structure and AB structure $MoSe_2$ bilayer. (**D** to **F**) High-resolution HAADF-STEM images of $MoSe_2$ film of (D) AA stacking, (E) AB stacking, and (F) grain boundary region.

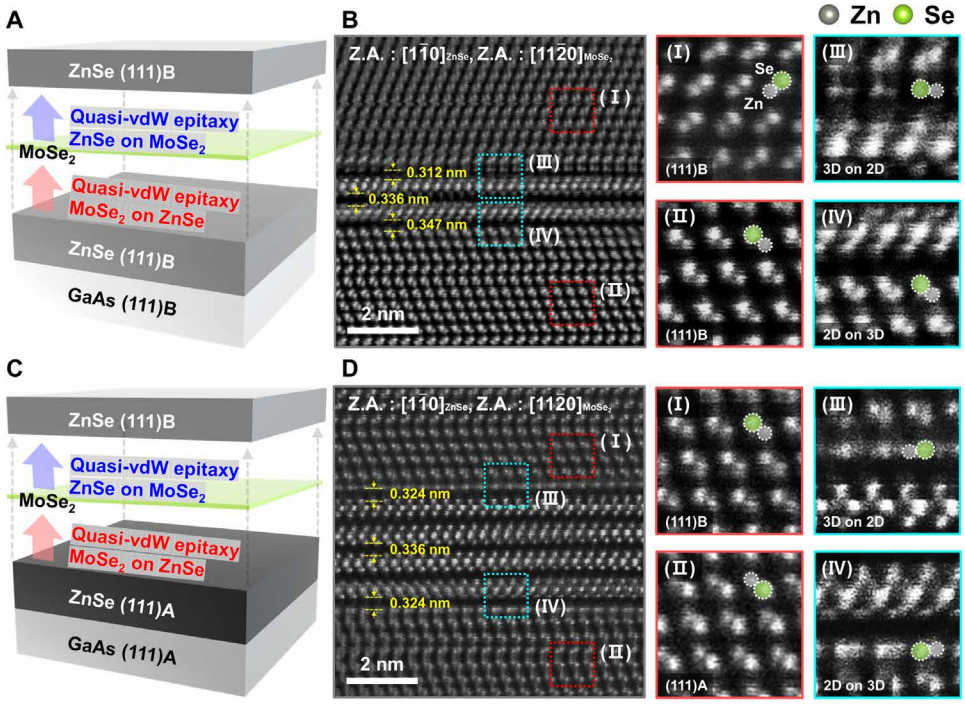


Fig. 4. Atomic-scale analysis of ZnSe/$MoSe_2$/ZnSe multidimensional heterointerface. (**A**) Schematic of polarities of ZnSe/$MoSe_2$/ZnSe MDH on GaAs (111)B. (**B**) Atomic-resolution cross-sectional HAADF-STEM image of the ZnSe/$MoSe_2$/ZnSe interface grown on GaAs (111)B viewed along the $[1\bar{1}0]_{ZnSe}$ zone axis. (**C**) Schematic of the QvdW epitaxy of $MoSe_2$ on ZnSe (111)A and ZnSe (111)B on $MoSe_2$. (**D**) Atomic-resolution cross-sectional HAADF-STEM image of ZnSe (111)B/$MoSe_2$/ZnSe (111)A interface grown on GaAs (111)A viewed along the $[1\bar{1}0]_{ZnSe}$ zone axis.

the presence of Zn vacancies (*42*, *45*), which is discussed again later. We infer that this interface reconstruction occurs due to the inability of ZnSe dangling bonds to bond with the $MoSe_2$ basal plane, which lacks dangling bonds, underscoring the unique interfacial dynamics between 2D and 3D materials. In addition, we observed that ZnSe on monolayer $MoSe_2$ exhibited the same epitaxial relationship, termination, and interface structure as on bilayer $MoSe_2$ (fig. S8). To investigate the factor influencing the lattice configuration of ZnSe on $MoSe_2$, we altered the termination of the GaAs (111) substrate from As-terminated (111)B to Ga-terminated (111)A and subsequently conducted ZnSe/$MoSe_2$/ZnSe MDH growth (Fig. 4C). Figure 4D presents a HAADF-STEM image of the ZnSe/$MoSe_2$/ZnSe MDH interface grown on a GaAs (111)A substrate. In this experiment, the $MoSe_2$ layer was grown under the same growth conditions as in the case of the (111)B substrate growth to facilitate a direct comparison. Despite identical growth conditions, the $MoSe_2$ layer on the (111)A substrate exhibited a greater thickness due to its higher growth rate. This difference in growth behavior is attributed to the stronger interaction between $MoSe_2$ and the ZnSe (111)A substrate, as indicated by our density functional theory (DFT) calculations, which show higher binding energies (discussed later in Fig. 5). Also, the bottom ZnSe layer exhibits a (111)A, Zn-terminated configuration, while the top ZnSe layer displays a (111)B, Se-terminated configuration. These observations suggest that the polarity of the top ZnSe layer is influenced not by the bottom ZnSe layer but rather by the $MoSe_2$ layer. Consequently, the epitaxial growth mode of the heterostructure is characterized as QvdW epitaxy, rather than remote epitaxy. Furthermore, both the top and bottom ZnSe monolayers at the interface manifest a buckling structure. This arises from the fact that the outermost atom species at the interface are Zn atoms, resulting in ZnSe (111)A–(2 × 2) reconstruction occurring at the 2D/3D interfaces. Notably, on the GaAs (111)A substrate, the QvdW gaps of ZnSe and $MoSe_2$ exhibit identical values, measured at 0.324 nm. This analysis affirms the interconnection between the substrate and the 2D/3D heterostructure polarity, as well as the development of interface structures during sequential MDH growth.

DFT calculation was performed to analyze the QvdW epitaxy mechanism governing the interaction between ZnSe and $MoSe_2$. For large-scale uniform growth of heterogeneous materials at the QvdW interface, the presence of preferential binding orientation is of importance. Using DFT calculations, we measure the binding energy between the ZnSe and $MoSe_2$ of different orientations, where the structure's lattice mismatch is below 2% to avoid strain effects' intervention (see table S1 for more details). Large thermal expansion coefficient mismatch can be a critical issue in heteroepitaxy; however, in our system, the small difference in in-plane thermal expansion coefficient between ZnSe and $MoSe_2$ reduces the potential for thermal strain (*46*, *47*). Therefore, our primary focus was on addressing the lattice mismatch between ZnSe and $MoSe_2$. At the single lattice scale, the lattice mismatch between ZnSe and $MoSe_2$ is determined to be 17.9% (Fig. 5, A and B). However, by adopting a commensurate supercell configuration comprising five ZnSe lattices and six $MoSe_2$ lattices, as confirmed through STEM analysis, the effective lattice mismatch is markedly reduced to 1.5% (Fig. 5C). Subsequently, the binding energy between ZnSe and $MoSe_2$ was calculated as a function of the angle between $[1\bar{1}0]_{ZnSe}$ direction and $[11\bar{2}0]_{MoSe2}$ direction for both $MoSe_2$ on ZnSe (111)

Downloaded from https://www.science.org at EWHA Womans University on May 25, 2025

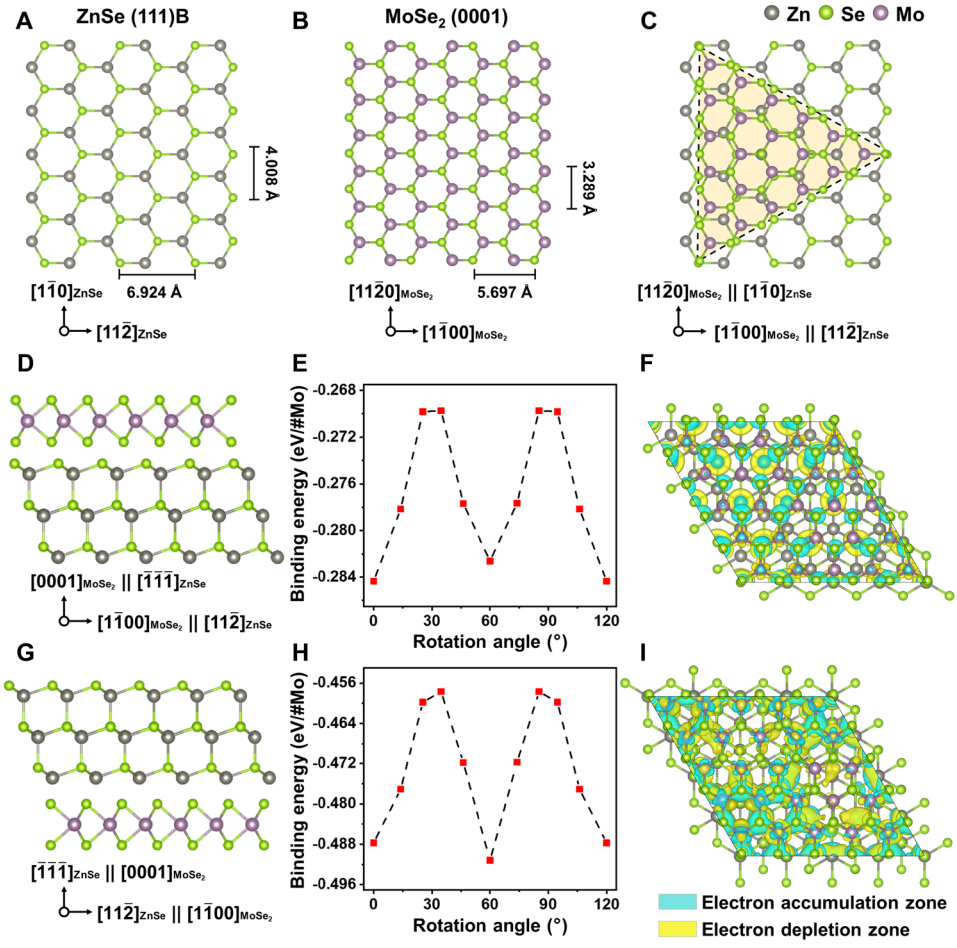


Fig. 5. Analysis of the QvdW epitaxy mechanism between ZnSe and $MoSe_2$ via DFT calculation. (**A** and **B**) Top views of (A) ZnSe (111)B and (B) $MoSe_2$ (0001). (**C**) Schematics of the epitaxial relationship between ZnSe and $MoSe_2$. (**D** to **F**) (D) Cross-sectional view, (E) binding energy as a function of the rotation angle, and (F) top view CDD plot of $MoSe_2$ on ZnSe (111)B. (**G** to **I**) (G) Cross-sectional view, (H) binding energy as a function of the rotation angle, and (I) top view CDD plot of ZnSe (111)B on $MoSe_2$.

B and ZnSe (111)B on $MoSe_2$ (Fig. 5, D and G, and table S1). The corresponding binding energy calculations for $MoSe_2$ on ZnSe (111)B and ZnSe (111)B on $MoSe_2$ are depicted in Fig. 5 (E and H), respectively. Notably, configurations at 0° and 60° exhibit the most stable binding energy values, aligning with experimental observations. Moreover, potential energy pits were not observed in between 0° and 60°, meaning no metastable orientation exists between the two mirror plane symmetric orientations. Top-view charge density difference (CDD) plots of $MoSe_2$ on ZnSe (111)B and ZnSe (111)B on $MoSe_2$ are presented in Fig. 5 (F and I), respectively. In these plots, the blue areas denote negatively charged electron accumulation zones, while the yellow areas represent positively charged electron depletion zones. The isosurface boundary value in the CDD plot is set at 0.001 e/bohr^3. While the interaction in the case of $MoSe_2$ on ZnSe (111)B does not exhibit notable electron exchange, a more pronounced electron exchange is observed in the case of ZnSe (111)B on $MoSe_2$, centered in regions where Zn and Se atoms are in close proximity. Quantitatively, ZnSe (111)B on $MoSe_2$ demonstrates a more stable binding energy compared to $MoSe_2$ on ZnSe (111)B. Formation of such periodic regions is expected as the ratio of the lattice parameters of ZnSe and $MoSe_2$ is 5:6, resulting in Moiré patterns. Because of this Moiré structure, a slightly stronger electron exchange occurs at the part where Zn and Se of $MoSe_2$ are in close contact.

The delamination behavior analysis was conducted by changing the types of elements at the interface. The position of the $MoSe_2$ layer was confirmed through Raman spectroscopy on both the delaminated film and the remaining substrate. Initially, characteristic Raman signals of both ZnSe and $MoSe_2$ were detected in the as-grown heterostructure sample (Fig. 2B). Figure 6A is a schematic of the delamination behavior of the ZnSe/$MoSe_2$/ZnSe MDH on GaAs (111)B. After delaminating ZnSe/$MoSe_2$ film, Raman spectroscopy was conducted on the remaining substrate. Notably, no signal related to $MoSe_2$ was detected in the remaining substrate, indicating complete separation of all $MoSe_2$ from the substrate during the delamination process (Fig. 6B). Subsequently, the delaminated film was transferred onto a SiO_2/Si substrate (fig. S9). The Raman spectrum for transferred film on SiO_2/Si substrate is shown in Fig. 6C. As the substrate changed from GaAs to SiO_2/Si, the Raman signal of GaAs disappeared and that of Si appeared. The signals of ZnSe and $MoSe_2$ are detected, indicating that both ZnSe and $MoSe_2$ are transferred on SiO_2/Si substrate. Through Raman analysis, we

Downloaded from https://www.science.org at EWHA Womans University on May 25, 2025

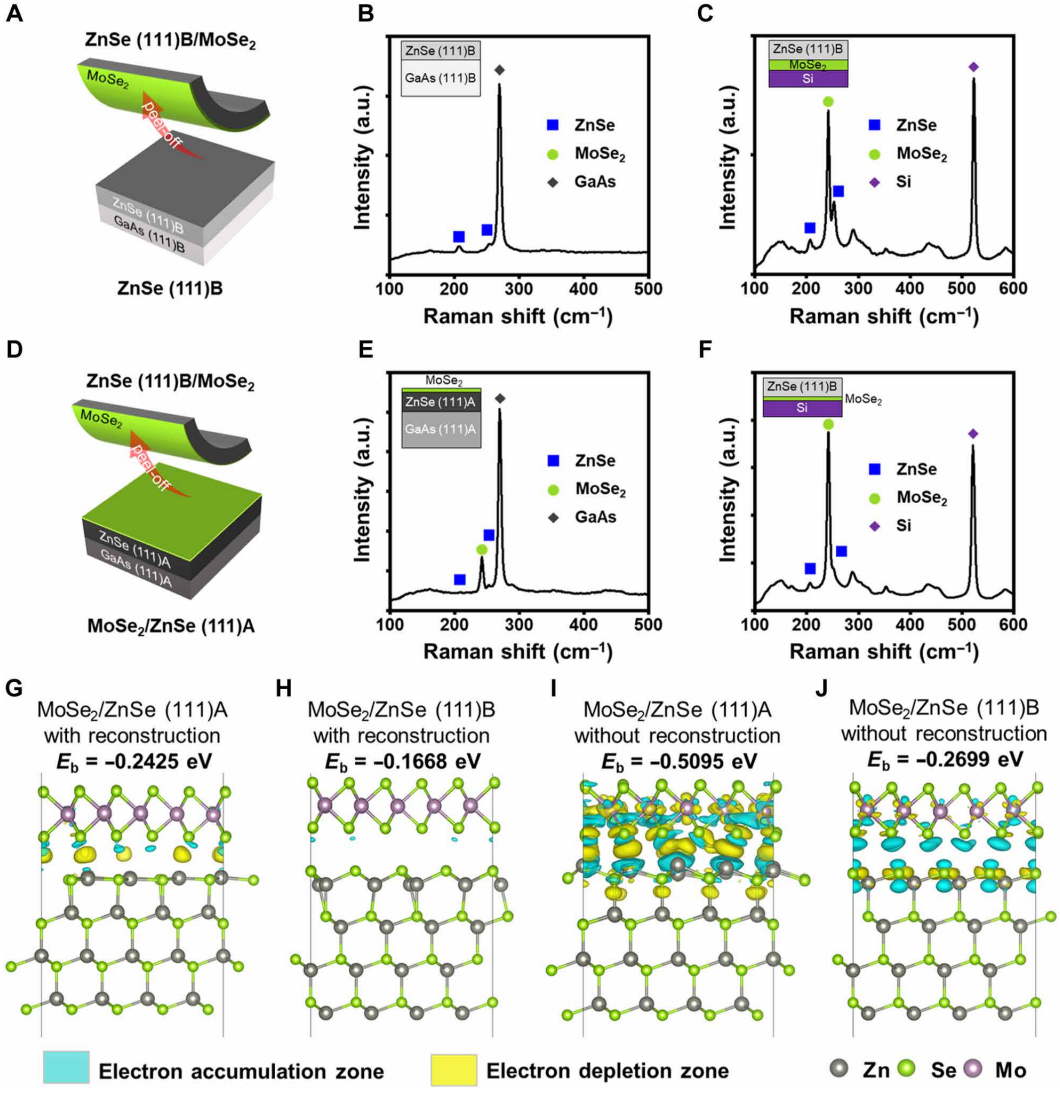


Fig. 6. Delamination behavior analysis through interface engineering. (**A**) Schematic of delamination behavior of ZnSe/$MoSe_2$ film from ZnSe (111)B substrate. (**B** and **C**) Raman spectrum of (B) the remaining ZnSe on GaAs (111)B substrate and (C) the transferred ZnSe/$MoSe_2$ film on SiO_2/Si. (**D**) Schematic of delamination behavior of ZnSe/$MoSe_2$ film from $MoSe_2$/ZnSe (111)A substrate. (**E** and **F**) Raman spectrum of (E) the remaining $MoSe_2$/ZnSe on GaAs (111)A substrate and (F) the transferred ZnSe/$MoSe_2$ film on SiO_2/Si. (**G** to **J**) CDD image of (G) $MoSe_2$/ZnSe (111)A (Se-Zn) interface with reconstruction, (H) $MoSe_2$/ZnSe (111)B (Se-Se) interface with reconstruction, (I) $MoSe_2$/ZnSe (111)A (Se-Zn) interface without reconstruction, and (J) $MoSe_2$/ZnSe (111)B (Se-Se) interface without reconstruction, with the value of the isosurface boundary being 0.001 e/bohr^3.

confirm that in the ZnSe/$MoSe_2$/ZnSe on GaAs (111)B sample, all $MoSe_2$ is detached from the substrate during the delamination process. Similarly, the presence of ZnSe and $MoSe_2$ was confirmed in the ZnSe/$MoSe_2$/ZnSe on GaAs (111)A sample (fig. S10). Upon conducting the same delamination process on the ZnSe/$MoSe_2$/ZnSe on GaAs (111)A, Raman analysis of the remaining GaAs (111)A substrate revealed the retention of $MoSe_2$ on the substrate during the delamination process (Fig. 6E). Figure 6F is the Raman spectra of the film delaminated from the ZnSe/$MoSe_2$/ZnSe on GaAs (111)A and transferred on the SiO_2/Si substrate. Detection of both ZnSe and $MoSe_2$ peaks suggests that, like in the ZnSe/$MoSe_2$/ZnSe on GaAs (111)B case, the ZnSe/$MoSe_2$ film delaminated from the substrate; however, the delamination occurred at a different interface (Fig. 6D).

To elucidate this delamination behavior, we begin by analyzing the possible interfacial states of the ZnSe/$MoSe_2$ system. The ZB (111)A surface often exhibits (2 × 2) reconstructions, characterized by vacancies forming in one of every four surface metal sites. Previous studies have also proposed trimer B atoms on the ZB (111)B surfaces and unreconstructed surfaces depending on the process conditions (*48*, *49*). Thus, we use a simulation cell with a ZnSe to $MoSe_2$ ratio of 4:5 and calculate the stability of surfaces with different vacancy ratios, varying the number of Zn vacancies from 0 to 4 (corresponding to a monolayer concentration of 0 to 0.25) on a 4 ZnSe lattice, which leads up to the formation of a (2 × 2) reconstruction. Our findings indicate that under most conditions, the (2 × 2) reconstructed configuration (0.25 ml) is advantageous on the ZB (111)A, both at the bare ZnSe surface and at the $MoSe_2$ interface

Downloaded from https://www.science.org at EWHA Womans University on May 25, 2025

(fig. S11, A and B). Note that the interface structure shows the equilibrium point shifted toward positive Zn chemical potential, due to stabilization of the surface energy provided by the interaction with $MoSe_2$. In addition, we observe that under Zn-rich conditions, surfaces with fewer vacancies (0.1825 ml) are more stable, hinting a lower vacancy containing reconstructions may be present. On the ZB (111)B surface and interface, we have determined that various Se vacancies are also likely to be present which serve to diminish the intrinsic polarity of the ZnSe surface and thus stabilize it (fig. S11, C and D). To further explore these surface reconstructions, we reevaluated the binding energies of these vacancy-induced surfaces in contact with the $MoSe_2$. Figure 6 (G to J) presents CCD plots of the (2 × 2) reconstructed $MoSe_2$/Zn-terminated ZnSe (111)A (Se-Zn interface), $MoSe_2$/Se-terminated ZnSe (111)B (Se-Se interface), $MoSe_2$/Zn-terminated ZnSe (111)A (Se-Zn interface) without Zn vacancy generation, and $MoSe_2$/Se-terminated ZnSe (111)B (Se-Se interface) without Se vacancy generation, respectively. While the binding energy of the pristine Zn-terminated and Se-terminated surfaces are −0.503 and −0.270 eV, respectively, the reconstructed surfaces manifest weaker binding energies, as summarized in table S2. This is not unexpected, as surface reconstruction leads to the stabilization of the surface energy, reducing dangling bonds and reactivity. From the CDD plots, the electron transfer is more active at the Zn-terminated interface, whereas little to no transfer is observed at the Se-terminated interface. After surface reconstruction, both Zn-terminated and Se-terminated interfaces show less electron transfer, signaling the relaxation of the ZnSe surface with reduced polarity. These results are consistent with our observations in delamination of ZnSe/$MoSe_2$/ZnSe on GaAs (111)B, where the $MoSe_2$ is detected only on the Zn-terminated interface. The interlayer distances (table S2) are also consistent with the STEM measurements in Fig. 4B. Where the weakly binding interface generally shows longer interlayer distances.

Comparing the binding of the $MoSe_2$/$MoSe_2$ interface with the $MoSe_2$/Se-terminated ZnSe interface, our DFT calculations indicate the strongest binding energy at the $MoSe_2$/$MoSe_2$ interface, at −0.3228 eV/Mo (fig. S12). This binding strength is greater than that observed on all Se-terminated interfaces and on most Zn-terminated interfaces under various vacancy conditions, except for the completely unreconstructed Zn-terminated interface. This finding appears contradictory to experimental observations where $MoSe_2$ was detected on both the delaminated and remaining ZnSe layers in the ZnSe/$MoSe_2$/ZnSe on the GaAs (111)A structure, indicating that delamination occurs at the $MoSe_2$/$MoSe_2$ interface. This contradiction may stem from several factors that are not adequately captured by our DFT model where we have simplified the structure to ZnSe/$MoSe_2$ and $MoSe_2$/$MoSe_2$ systems of infinite periodic planes, whereas in reality, grain boundaries of different stacking exist as in Fig. 3F, which may lead to local structural deviation from perfect stacking of the $MoSe_2$ layers, weakening the interlayer binding. Moreover, binding energies obtained by DFT, while effectively highlighting the enthalpic interactions at optimized interfaces, serve as reference descriptors to the delamination process, where in reality, thermal fluctuations and mechanical stress also contribute to the physical delamination. For example, it is known that the binding energy of the transition metal dichalcogenide bilayer is highly dependent on the stacking mode, where the less stable stacking mode has as much as ~0.106 electron volts per formula units (eV/f.u.) weaker binding energies. Such phenomena indicate that microscopic shear sliding induced in the delamination process can weaken the interlayer binding at the $MoSe_2$ interface when strain, thermal, and entropic effects are considered. This phenomenon highlights a critical area for further research, as exploring these effects could lead to a deeper understanding of the mechanical stability and integrity of layered materials under real-world operational conditions.

DISCUSSION

In summary, we present the fabrication of Se-sharing ZnSe/$MoSe_2$/ZnSe MDH on GaAs (111) substrates using sequential MOCVD. The motivation for studying this specific structure stems from our aim to deepen the fundamental understanding of 2D/3D QvdW epitaxy in creating high-quality interfaces between 2D materials and 3D materials. By selecting Se-sharing ZnSe and $MoSe_2$ material combinations, we minimized interfacial reactions and chalcogen vacancy formation, ensuring the formation of sharp, high-quality heterointerfaces. The transfer-free sequential MOCVD growth and immiscible Se-based material combinations allowed us to establish a robust platform for analyzing MDH with high-quality interfaces. Through comprehensive analysis using HAADF-STEM and DFT calculations, we elucidate the epitaxial relationship and interface properties of the MDH. Both $MoSe_2$ on ZnSe and ZnSe on $MoSe_2$ exhibit identical epitaxial relationships of $(\bar{1}\bar{1}\bar{1})[1\bar{1}0]_{ZnSe}||(0001)[11\bar{2}0]_{MoSe2}$. Interface engineering strategies, supported by DFT calculations, confirm the QvdW epitaxy of ZnSe on $MoSe_2$ and reveal insights into delamination behavior driven by interfacial interactions. Notably, the Zn-Se atomic interface demonstrates stronger interaction compared to the Se-Se atomic interface, attributed to differences in electronegativity. Expanding beyond the ZnSe/$MoSe_2$ system, our study highlights the versatility of using various 2D/3D combinations, offering promising prospects for diverse applications. For example, since ZnSe and ZnS can be epitaxially grown on Si and Ge due to their crystal matching, this allows seamless integration into Si complementary metal-oxide semiconductor architectures, including gate-all-around field-effect transistors, where 2D materials serve as channel materials. Moreover, the ease of controlling chalcogen vacancies in gate stack interlayers, facilitated by chalcogen compound–based channels instead of oxides, presents opportunities for gate stack interlayer engineering, enhancing device performance. Furthermore, our work uniquely implements QvdW/vdW/QvdW heterostructures, achieving a true heterovalent architecture of 3D/2D/3D interfaces. This combination of QvdW and vdW interfaces in a single architecture is unprecedented, opening previously unexplored research avenues and technological opportunities.

MATERIALS AND METHODS

Sequential MOCVD growth of ZnSe/$MoSe_2$/ZnSe on GaAs (111)

ZnSe/$MoSe_2$/ZnSe MDH was grown on GaAs (111) substrate using homemade horizontal hot wall MOCVD. Before growth on the GaAs (111) substrate, the substrate was treated with HCl:deionized water (1:1) solution for 1 min to remove native oxides on the substrate. After then, the substrate was soaked in the deionized water for 1 min to rinse the residual HCl solution. $(C_2H_5)_2Zn$ (Sigma-Aldrich, 256781), $Mo(CO)_6$ (Sigma-Aldrich, 577766), and $(CH_3)_2Se$

Downloaded from https://www.science.org at EWHA Womans University on May 25, 2025

(Alfa Aesar, 068116) were used as Zn, Mo, and Se precursors, respectively (*50*). The injection of each precursor was controlled using mass flow controllers and maintained at room temperature, except for the molybdenum precursor, which was kept at 60°C to increase the vaporization of the precursor. All growth processes were carried out at 500°C. The optimized growth condition of the lower ZnSe layer on GaAs (111) is 2.0 standard cubic centimeter per minute (SCCM) for $(C_2H_5)_2Zn$, 0.5 SCCM for $(CH_3)_2Se$ with 125 SCCM of Ar carrier gas, and 9 SCCM of H_2 under 20 torr. After ZnSe layer growth, the purging process was carried out with 125 SCCM of Ar carrier gas for 10 min. The $MoSe_2$ layer was grown at the optimized conditions of 370 SCCM of Ar, 5 SCCM of H_2, 1.8 SCCM of $Mo(CO)_6$, and 0.4 SCCM of $(CH_3)_2Se$ under 2.5 torr. After 10 min of purging process, the upper ZnSe layer was grown with 2.2 SCCM $(C_2H_5)_2Zn$, 0.5 SCCM $(CH_3)_2Se$, 3 SCCM H_2, and 125 SCCM Ar under 20 torr.

Layer delamination and transfer

The ZnSe/$MoSe_2$/ZnSe MDH film was coated by spin coater with poly(methyl methacrylate) (PMMA; molecular weight 950,000, Microchem) at 4000 rpm for 30 s. The spin-coated sample was baked at 180°C for 10 min using a hot plate. After annealing, TRT was attached to PMMA/ZnSe/$MoSe_2$/ZnSe on the GaAs (111) sample. The TRT/PMMA/ZnSe/$MoSe_2$ film is separated from the substrate via mechanical peeling. The TRT/PMMA/ZnSe/$MoSe_2$ film was transferred on SiO_2/Si substrate using a vacuum stacking process (*51*). The TRT film was removed at 150°C on the hot plate. The transferred film was annealed at 180°C for 2 hours in a box furnace under N_2 atmosphere. Then, PMMA was removed by acetone overnight, and this was followed by cleaning with isopropyl alcohol (IPA) and blowing with N_2 gas.

Twinned QvdW epitaxially grown $MoSe_2$ film sampling process for top view TEM

The $MoSe_2$/ZnSe heterostructure on GaAs (111)B was prepared using the same growth process, except for the top ZnSe layer growth step. For the ZnSe etchant, citric acid crystals were dissolved in deionized water at room temperature at a ratio of 100 g of $C_6H_8O_7$ to 100 ml of deionized water. This citric acid solution was mixed with 30% hydrogen peroxide at a volume ratio of 3:1. The $MoSe_2$/ZnSe/GaAs sample was placed on the surface of the etchant solution. After etching the ZnSe layer, the floating $MoSe_2$ was carefully washed with deionized water. The $MoSe_2$ film was then scooped up and transferred onto a holey carbon TEM grid.

Characterization

The surface morphology of ZnSe/$MoSe_2$/ZnSe MDH was characterized using field-emission scanning electron microscopy (SEM; Hitachi S-4800) and atomic force microscopy (Park Systems NX-10). The crystalline plane and phases were confirmed by XRD (Rigaku Smartlab) with Cu Kα incident beam and micro-Raman spectroscopy (Horiba Aramis) with a 514-nm excitation laser source. In-plane orientation was measured by HR-XRD (Panalytical X'pert MRD) with a four-crystal Ge (220) monochromator and EBSD (Thermo Fisher Scientific Quattro SEM). The cross-sectional samples for STEM imaging were prepared by a focused ion beam (NX2000 Hitachi). The atomic-resolution cross-sectional images were obtained using FEI Titan3 G2 60-300 with an operating voltage of 200 kV.

Computational calculation methods

All DFT calculations were performed using Vienna Ab-initio Software Package (VASP, version 6.2.0). For the exchange-correlation functional, Perdew-Burke-Ernzerhof (PBE) was used, along with D3 correction with Becke-Johnson (BJ) damping to account for the dispersion interaction between the vdW materials (*52*–*56*). A cut-off energy of 400 eV was used, with γ-centered automatic *k*-point grid spacing of 0.2 A^{-1}, to account for the various supercells used. The electronic convergence criterion of 1×10^{-5} eV and the force convergence criterion of 0.01 eV/Å were used for geometric convergence. For computational efficiency, ZnSe three bilayer slabs were used for binding energy according to epitaxial direction. For other properties, four bilayer slabs were used, all with two bottom bilayers fixed to the bulk configuration. Interaction energy between the ZnSe and the $MoSe_2$ monolayer was calculated by the formula

$$\Delta E_{\text{binding}} = \left(E_{\text{MoSe}_2-\text{ZnSe}} + E_{\text{MoSe}_2} - E_{\text{ZnSe}}\right) / n$$

where n is the number of Mo units in the simulation cell and $E_{\text{MoSe}_2-\text{ZnSe}}$, E_{MoSe_2}, and E_{ZnSe} are the energies of the interface structure, free-standing $MoSe_2$, and ZnSe, respectively. Visualization for Electronic and Structural Analysis (VESTA) was used for visualization of the charge densities (*57*).

Supplementary Materials

This PDF file includes:

Figs. S1 to S12
Tables S1 to S3

REFERENCES AND NOTES

1. J. E. Ayers, *Heteroepitaxy of Semiconductors: Theory, Growth, and Characterization* (CRC Press, 2007).
2. A. W. Bett, F. Dimroth, G. Stollwerck, O. V. Sulima, III-V compounds for solar cell applications. *Appl. Phys. A* **69**, 119–129 (1999).
3. J. C. Norman, D. Jung, Z. Zhang, Y. Wan, S. Liu, C. Shang, R. W. Herrick, W. W. Chow, A. C. Gossard, J. E. Bowers, A review of high-performance quantum dot lasers on silicon. *IEEE J. Quantum Electron.* **55**, 1–11 (2019).
4. U. K. Mishra, P. Parikh, Y.-F. Wu, AlGaN/GaN HEMTs-an overview of device operation and applications. *Proc. IEEE* **90**, 1022–1031 (2002).
5. R. S. Pengelly, S. M. Wood, J. W. Milligan, S. T. Sheppard, W. L. Pribble, A review of GaN on SiC high electron-mobility power transistors and MMICs. *IEEE T. Microw. Theory* **60**, 1764–1783 (2012).
6. A. Koma, K. Sunouchi, T. Miyajima, Fabrication and characterization of heterostructures with subnanometer thickness. *Microelectron. Eng.* **2**, 129–136 (1984).
7. A. Koma, K. Sunouchi, T. Miyajima, Fabrication of ultrathin heterostructures with van der Waals epitaxy. *J. Vac. Sci. Technol. B* **3**, 724 (1985).
8. T. S. Kim, G. Noh, S. Kwon, J. Y. Kim, K. P. Dhakal, S. Oh, H. J. Chai, E. Park, I. S. Kim, E. Lee, Y. Kim, J. Lee, M. K. Jo, M. Kang, C. Park, J. Kim, J. Park, S. Kim, M. Kim, Y. Kim, S. Y. Choi, S. Song, H. Y. Jeong, J. Kim, J. Y. Kwak, K. Kang, Diffusion control on the van der Waals surface of monolayers for uniform Bi-layer MoS_2 growth. *Adv. Funct. Mater.* **34**, 2312365 (2024).
9. K. Ueno, T. Shimada, K. Saiki, A. Koma, Heteroepitaxial growth of layered transition metal dichalcogenides on sulfur-terminated GaAs{111} surfaces. *Appl. Phys. Lett.* **56**, 327–329 (1990).
10. A. Koma, K. Saiki, Y. Sato, Heteroepitaxy of a two-dimensional material on a three-dimensional material. *Appl. Surf. Sci.* **42**, 451–456 (1989).
11. A. Koma, Van der Waals epitaxy—A new epitaxial growth method for a highly lattice-mismatched system. *Thin Solid Films* **216**, 72–76 (1992).
12. P. Kumar, J. Lynch, B. Song, H. Ling, F. Barrera, K. Kisslinger, H. Zhang, S. B. Anantharaman, J. Digani, H. Zhu, T. H. Choudhury, C. McAleese, X. Wang, B. R. Conran, O. Whear, M. J. Motala, M. Snure, C. Muratore, J. M. Redwing, N. R. Glavin, E. A. Stach, A. R. Davoyan, D. Jariwala, Light–matter coupling in large-area van der Waals superlattices. *Nat. Nanotechnol.* **17**, 182–189 (2022).

Downloaded from https://www.science.org at EWHA Womans University on May 25, 2025

13. W. Cao, J. Jiang, J. Kang, D. Sarkar, W. Liu, K. Banerjee, Designing band-to-band tunneling field-effect transistors with 2D semiconductors for next-generation low-power VLSI, *IEEE International Electron Devices Meeting* 12.3.1–12.3.4 (2015).
14. W. Yan, O. Txoperena, R. Llopis, H. Dery, L. E. Hueso, F. Casanova, A two-dimensional spin field-effect switch. *Nat. Commun.* **7**, 13372 (2016).
15. A. Dankert, S. P. Dash, Electrical gate control of spin current in van der Waals heterostructures at room temperature. *Nat. Commun.* **8**, 16093 (2017).
16. J. Ingla-Aynés, F. Herling, J. Fabian, L. E. Hueso, F. Casanova, Electrical control of valley-zeeman spin-orbit-coupling-induced spin precession at room temperature. *Phys. Rev. Lett.* **127**, 047202 (2021).
17. J. Park, S. J. Kwak, S. Kang, S. Oh, B. Shin, G. Noh, T. S. Kim, C. Kim, H. Park, S. H. Oh, W. Kang, N. Hur, H. J. Chai, M. Kang, S. Kwon, J. Lee, Y. Lee, E. Moon, C. Shi, J. Lou, W. B. Lee, J. Y. Kwak, H. Yang, T. M. Chung, T. Eom, J. Suh, Y. Han, H. Y. Jeong, Y. J. Kim, K. Kang, Area-selective atomic layer deposition on 2D monolayer lateral superlattices. *Nat. Commun.* **15**, 2138 (2024).
18. W. Meng, F. Xu, Z. Yu, T. Tao, L. Shao, L. Liu, T. Li, K. Wen, J. Wang, L. He, L. Sun, W. Li, H. Ning, N. Dai, F. Qin, X. Tu, D. Pan, S. He, D. Li, Y. Zheng, Y. Lu, B. Liu, R. Zhang, Y. Shi, X. Wang, Three-dimensional monolithic micro-LED display driven by atomically thin transistor matrix. *Nat. Nanotechnol.* **16**, 1231–1236 (2021).
19. J. H. Kang, H. Shin, K. S. Kim, M. K. Song, D. Lee, Y. Meng, C. Choi, J. M. Suh, B. J. Kim, H. Kim, A. T. Hoang, B. I. Park, G. Zhou, S. Sundaram, P. Vuong, J. Shin, J. Choe, Z. Xu, R. Younas, J. S. Kim, S. Han, S. Lee, S. O. Kim, B. Kang, S. Seo, H. Ahn, S. Seo, K. Reidy, E. Park, S. Mun, M. C. Park, S. Lee, H. J. Kim, H. S. Kum, P. Lin, C. Hinkle, A. Ougazzaden, J. H. Ahn, J. Kim, S. H. Bae, Monolithic 3D integration of 2D materials-based electronics towards ultimate edge computing solutions. *Nat. Mater.* **22**, 1470–1477 (2023).
20. N. Cavassilas, D. Logoteta, Y. Lee, F. Michelini, M. Lannoo, M. Bescond, M. Luisier, Dual-gated $WTe_2/MoSe_2$ van der Waals tandem solar cells. *J. Phys. Chem. C* **122**, 28545–28549 (2018).
21. D. Jariwala, A. R. Davoyan, J. Wong, H. A. Atwater, Van der Waals materials for atomically-thin photovoltaics: Promise and outlook. *ACS Photonics* **4**, 2962–2970 (2017).
22. E. Singh, K. S. Kim, G. Y. Yeom, H. S. Nalwa, Atomically thin-layered molybdenum disulfide (MoS_2) for bulk-heterojunction solar cells. *ACS Appl. Mater. Interfaces* **9**, 3223–3245 (2017).
23. K. S. Kim, J. Kwon, H. Ryu, C. Kim, H. Kim, E. K. Lee, D. Lee, S. Seo, N. M. Han, J. M. Suh, J. Kim, M. K. Song, S. Lee, M. Seol, J. Kim, The future of two-dimensional semiconductors beyond Moore's law. *Nat. Nanotechnol.* **19**, 895–906 (2024).
24. Y. Wang, S. Sarkar, H. Yan, M. Chhowalla, Critical challenges in the development of electronics based on two-dimensional transition metal dichalcogenides. *Nat. Electron.* **7**, 638–645 (2024).
25. Y. Kim, W. J. Woo, D. Kim, S. Lee, S. min Chung, J. Park, H. Kim, Atomic-layer-deposition-based 2D transition metal chalcogenides: Synthesis, modulation, and applications. *Adv. Mater.* **33**, e2005907 (2021).
26. Q. Qian, B. Li, M. Hua, Z. Zhang, F. Lan, Y. Xu, R. Yan, K. J. Chen, Improved gate dielectric deposition and enhanced electrical stability for single-layer MoS_2 MOSFET with an AlN interfacial layer. *Sci. Rep.* **6**, 27676 (2016).
27. P. Gupta, A. A. Rahman, S. Subramanian, S. Gupta, A. Thamizhavel, T. Orlova, S. Rouvimov, S. Vishwanath, V. Protasenko, M. R. Laskar, H. G. Xing, D. Jena, A. Bhattacharya, Layered transition metal dichalcogenides: Promising near-lattice-matched substrates for GaN growth. *Sci. Rep.* **6**, 23708 (2016).
28. Y. Yin, B. Liu, Q. Chen, Z. Chen, F. Ren, S. Zhang, Z. Liu, R. Wang, M. Liang, J. Yan, J. Sun, X. Yi, T. Wei, J. Wang, J. Li, Z. Liu, P. Gao, Z. Liu, Continuous single-crystalline GaN film grown on WS_2-glass wafer. *Small* **18**, e2202529 (2022).
29. Y. Chen, Z. Shi, S. Zhang, J. Ben, K. Jiang, H. Zang, Y. Jia, W. Lü, D. Li, X. Sun, The van der Waals epitaxy of high-quality N-polar gallium nitride for high-response ultraviolet photodetectors with polarization electric field modulation. *Adv. Electron. Mater.* **8**, 2100759 (2022).
30. D. Ruzmetov, K. Zhang, G. Stan, B. Kalanyan, G. R. Bhimanapati, S. M. Eichfeld, R. A. Burke, P. B. Shah, T. P. O'Regan, F. J. Crowne, A. G. Birdwell, J. A. Robinson, A. V. Davydov, T. G. Ivanov, Vertical 2D/3D semiconductor heterostructures based on epitaxial molybdenum disulfide and gallium nitride. *ACS Nano* **10**, 3580–3588 (2016).
31. F. Liu, T. Wang, Z. Zhang, T. Shen, X. Rong, B. Sheng, L. Yang, D. Li, J. Wei, S. Sheng, X. Li, Z. Chen, R. Tao, Y. Yuan, X. Yang, F. Xu, J. Zhang, K. Liu, X. Z. Li, B. Shen, X. Wang, Lattice polarity manipulation of quasi-vdW epitaxial GaN films on graphene through interface atomic configuration. *Adv. Mater.* **34**, e2106814 (2022).
32. D. M. Geum, S. Kim, J. H. Khym, J. Lim, S. K. Kim, S. Y. Ahn, T. S. Kim, K. Kang, S. H. Kim, Arrayed MoS_2–$In_{0.53}Ga_{0.47}As$ van der Waals heterostructure for high-speed and broadband detection from visible to shortwave-infrared light. *Small* **17**, e2007357 (2021).
33. A. Jain, S. P. Ong, G. Hautier, W. Chen, W. D. Richards, S. Dacek, S. Cholia, D. Gunter, D. Skinner, G. Ceder, K. A. Persson, Commentary: The materials project: A materials genome approach to accelerating materials innovation. *APL Mater.* **1**, 011002 (2013).
34. S. P. Ong, L. Wang, B. Kang, G. Ceder, Li - Fe - P - O_2 phase diagram from first principles calculations. *Chem. Mater.* **20**, 1798–1807 (2008).
35. M. A. Herman, W. Richter, H. Sitter, *Epitaxy: Physical Principles and Technical Implementation* (Springer Science & Business Media, 2013), vol. 62.
36. V. L. Tassev, Heteroepitaxy, an amazing contribution of crystal growth to the world of optics and electronics. *Crystals* **7**, 178 (2017).
37. J. Xu, A. Lu, C. Wang, R. Zou, X. Liu, X. Wu, Y. Wang, S. Li, L. Sun, X. Chen, H. Oh, H. Baek, G. C. Yi, J. Chu, ZnSe-based longitudinal twinning nanowires. *Adv. Eng. Mater.* **16**, 459–465 (2014).
38. C. T. Wu, S. Y. Hu, K. K. Tiong, Y. C. Lee, Anisotropic effects in the Raman scattering of Re-doped 2H-$MoSe_2$ layered semiconductors. *Res. Phys.* **7**, 4096–4100 (2017).
39. A. G. Kontos, N. Chrysanthakopoulos, M. Calamiotou, T. Kehagias, P. Komninou, U. W. Pohl, Structural properties of ZnSe epilayers on (111) GaAs. *J. Appl. Phys.* **90**, 3301–3307 (2001).
40. S. Rubini, B. Bonanni, E. Pelucchi, A. Franciosi, A. Garulli, A. Parisini, Y. Zhuang, G. Bauer, V. Holý, ZnSe/CdTe/ZnSe heterostructures. *J. Vac. Sci. Technol. B* **18**, 2263–2270 (2000).
41. S. Mukherjee, N. Nateghi, R. M. Jacobberger, E. Bouthillier, M. de la Mata, J. Arbiol, T. Coenen, D. Cardinal, P. Levesque, P. Desjardins, R. Martel, M. S. Arnold, O. Moutanabbir, Growth and luminescence of polytypic InP on epitaxial graphene. *Adv. Funct. Mater.* **28**, 1705592 (2018).
42. Y. J. Hong, J. W. Yang, W. H. Lee, R. S. Ruoff, K. S. Kim, T. Fukui, Van der Waals epitaxial double heterostructure: InAs/single-layer graphene/InAs. *Adv. Mater.* **25**, 6847–6853 (2013).
43. A. Ohtake, Y. Sakuma, Effect of substrate orientation on $MoSe_2$/GaAs heteroepitaxy. *J. Phys. Chem. C* **124**, 5196–5203 (2020).
44. D. E. Jesson, S. J. Pennycook, Incoherent imaging of crystals using thermally scattered electrons. *Proc. R. Soc. Lond. A.* **449**, 273–293 (1995).
45. V. L. Bekenev, S. M. Zubkova, Atomic and electron structure of reconstructed (111) surface in ZnSe and CdSe crystals. *Phys. Solid State* **60**, 191–206 (2018).
46. C. H. Su, S. Feth, S. L. Lehoczky, Thermal expansion coefficient of ZnSe crystal between 17 and 1080 °C by interferometry. *Mater. Lett.* **63**, 1475–1477 (2009).
47. S. H. El-Mahalawy, B. L. Evans, The thermal expansion of 2H-MoS_2, 2H-$MoSe_2$ and 2H-WSe_2 between 20 and 800°C. *J. Appl. Crystallogr.* **9**, 403–406 (1976).
48. A. Ohtake, J. Nakamura, T. Komura, T. Hanada, T. Yao, H. Kuramochi, M. Ozeki, Surface structures of GaAs{111}A,B-(2 × 2). *Phys. Rev. B.* **64**, 045318 (2001).
49. Z. Liu, C. Merckling, R. Rooyackers, O. Richard, H. Bender, Y. Mols, M. Vila, J. Rubio-Zuazo, G. R. Castro, N. Collaert, A. Thean, W. Vandervorst, M. Heyns, Correlation between surface reconstruction and polytypism in InAs nanowire selective area epitaxy. *Phys. Rev. Mater.* **1**, 074603 (2017).
50. T. S. Kim, K. P. Dhakal, E. Park, G. Noh, H. J. Chai, Y. Kim, S. Oh, M. Kang, J. Park, J. Kim, S. Kim, H. Y. Jeong, S. Bang, J. Y. Kwak, J. Kim, K. Kang, Gas-phase alkali metal-assisted MOCVD growth of 2D transition metal dichalcogenides for large-scale precise nucleation control. *Small* **18**, e2106368 (2022).
51. K. Kang, K. H. Lee, Y. Han, H. Gao, S. Xie, D. A. Muller, J. Park, Layer-by-layer assembly of two-dimensional materials into wafer-scale heterostructures. *Nature* **550**, 229–233 (2017).
52. G. Kresse, J. Furthmüller, Efficient iterative schemes for ab initio total-energy calculations using a plane-wave basis set. *Phys. Rev. B* **54**, 11169–11186 (1996).
53. G. Kresse, J. Furthmüller, Efficiency of ab-initio total energy calculations for metals and semiconductors using a plane-wave basis set. *Comput. Mater. Science* **6**, 15–50 (1996).
54. J. P. Perdew, K. Burke, M. Ernzerhof, Generalized gradient approximation made simple. *Phys. Rev. Lett.* **77**, 3865–3868 (1996).
55. S. Grimme, J. Antony, S. Ehrlich, H. Krieg, A consistent and accurate *ab initio* parametrization of density functional dispersion correction (DFT-D) for the 94 elements H-Pu. *J. Chem. Phys.* **132**, 154104 (2010).
56. S. Grimme, S. Ehrlich, L. Goerigk, Effect of the damping function in dispersion corrected density functional theory. *J. Comput. Chem.* **32**, 1456–1465 (2011).
57. K. Momma, F. Izumi, VESTA 3 for three-dimensional visualization of crystal, volumetric and morphology data. *J. Appl. Crystallogr.* **44**, 1272–1276 (2011).

Acknowledgments

Funding: This research was supported by the National R&D Program through the National Research Foundation of Korea (NRF) funded by Ministry of Science and ICT (2022M3H4A1A01013228, 2022M3H4A1A01010325, RS-2023-00258309, and 2022M3F3A2A01072215). Additional support was provided by the Korea Institute for Advancement of Technology (KIAT) grant, funded by the Korea Government (MOTIE) (P0023708, HRD Program for Industrial Innovation). This work was also supported by the Samsung Science and Technology Foundation (0414-20240187). **Author contributions:** Conceptualization: S.K. and K.K. Methodology: S.K., S.O., S.J.K., M.C., and K.K. Investigation: S.K., S.O., S.J.K., J.L., M.-g.K., T.S.K., M.-k.J., and K.K. Visualization: S.K., S.O., S.J.K., G.N., and K.K. Supervision: G.N., J.Y., Y.J.H., S.S., J.Y.K., YongJoo K., H.Y.J., and K.K. Writing—original draft: S.K. and K.K. Writing—review and editing: S.K., S.O., S.J.K., G.N., M.C., J.L., Yuseok K., M.-g.K., T.S.K., M.-k.J., W.B.L., J.Y., Y.J.H., S.S., J.Y.K., H.Y.J., YongJoo K., and K.K. **Competing interests:** The authors declare that they have no competing interests. **Data and materials availability:** All data needed to evaluate the conclusions in the paper are present in the paper and/or the Supplementary Materials.

Submitted 14 August 2024
Accepted 21 January 2025
Published 21 February 2025
10.1126/sciadv.ads4573

Downloaded from https://www.science.org at EWHA Womans University on May 25, 2025